special communication

Four-dimensional imaging of living chondrocytes in cartilage using confocal microscopy: a pragmatic approach

RACHEL J. ERRINGTON,[1] MARK D. FRICKER,[2] JULIAN L. WOOD,[2]
ANDREW C. HALL,[1] AND NICK S. WHITE[2]
[1]*Department of Physiology, University of Oxford, Oxford OX1 3PT; and*
[2]*Department of Plant Sciences, University of Oxford, Oxford OX1 3RB, United Kingdom*

Errington, Rachel J., Mark D. Fricker, Julian L. Wood, Andrew C. Hall, and Nick S. White. Four-dimensional imaging of living chondrocytes in cartilage using confocal microscopy: a pragmatic approach. *Am. J. Physiol.* 272 (*Cell Physiol.* 41): C1040–C1051, 1997.—Regulation of cell volume is a fundamental cellular homeostatic mechanism in the face of osmotic stress. In normal articular cartilage, chondrocytes are exposed to a changing osmotic environment. We present a comprehensive protocol for studying the volume regulatory behavior of chondrocytes within intact cartilage tissue using confocal laser-scanning microscopy. Our data acquisition regime optimizes both signal-to-noise and cell viability during time-lapsed three-dimensional (3-D) (x, y, z, t) imaging. The porcine cartilage is treated as an integrated component of the imaging system, and we demonstrate methods for the direct assessment of tissue-induced axial attenuation and image distortion. Parameterized functions describing these two components of image degradation are used to correct experimental data. The current study also highlights the problems associated with the analysis and visualization of four-dimensional (4-D) images. We have devised two new types of data reconstruction. The first compresses each 3-D time point into a single quantitative view, termed a coordinate view. From these reconstructions we are able to simultaneously view and extract cell measurements. A second type, a 4-D reconstruction, uses color to represent relative changes in cell volume, again while maintaining the morphological and spatial information. Both these approaches of image analysis and visualization have been implemented to study the morphology, spatial distribution, and dynamic volume behavior of chondrocytes after osmotic perturbation. We have mapped chondrocyte shape, arrangement, and absolute volume in situ, which vary significantly from the tissue surface through to the underlying bone. Despite the rigid nature of the extracellular matrix, cartilage cells are osmotically sensitive and respond to stimulation of volume regulatory mechanisms. The combined techniques of confocal laser-scanning microscopy and vital cell labeling have enabled us to study, for the first time, the response of chondrocytes in situ to changes in interstitial osmotic pressure.

volume regulation

CHONDROCYTES, THE CELLS of articular cartilage, are situated within a tough extracellular matrix. The mechanical properties of this tissue are essential for normal joint function (18). Cartilage consists of two major components: collagen (specifically type II), which provides tensile strength, and proteoglycans for compressive strength (19, 23). The function of a chondrocyte is to manufacture and degrade the macromolecular extracellular matrix constituents, but the balance of matrix turnover is also determined by the external environment. Cartilage experiences complex mechanical forces in vivo (13, 18, 26). During a sustained load, fluid is expressed from the tissue, increasing the concentration of proteoglycans and extracellular cations. When load is removed, the tissue assumes a normal state of hydration. Thus chondrocytes are exposed to a dynamic ionic and osmotic environment. Potentially, chondrocytes exploit changes in extracellular mechanical and chemical information to modulate their physiological and metabolic behavior (1). Indeed, it has been shown that the osmotic and ionic environment influences matrix metabolism (28, 34); therefore, it is important to understand chondrocyte volume regulation in the face of such environmental challenges. It is currently unclear how a chondrocyte will respond to osmotic perturbations.

One approach to understanding aspects of chondrocyte volume regulation involves the removal of cells from the matrix and their manipulation in culture. Conventional methods for measuring dynamic volume changes require the isolation of cells from the tissue. However, when using these approaches, the three-dimensional (3-D) spatial organization of the tissue is lost as well as any corresponding local ionic gradients (17, 27, 30). This disturbance of the 3-D physical and chemical environment, together with the progressive dedifferentiation of the isolated chondrocytes, creates problems when relating the observed volume regulatory behavior to the physiology of intact cartilage tissue. The current study presents an alternative approach of in situ volume measurement by directly imaging living chondrocytes within intact cartilage explants. Noninvasive optical sectioning by confocal laser-scanning microscopy (CLSM) has enabled us to quantify dynamic changes of cell volume in response to an osmotic perturbation within the intact tissue. The "organ culture" system (8) we have used maintains tissue integrity and hence the spatial organization of chondrocytes in the extracellular matrix.

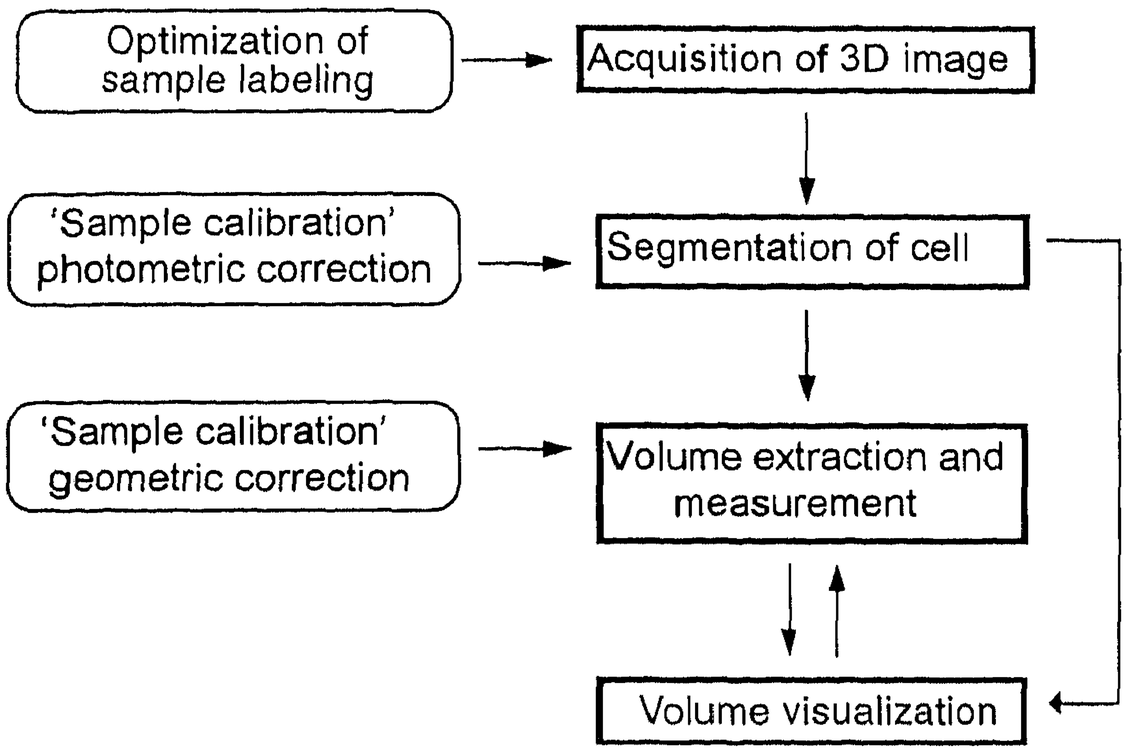

Fig. 1. Flow diagram representing the key stages of live cell volume imaging (square boxes). Each phase required optimization steps (rounded boxes) that were necessary to both extract and view chondrocyte volume in the tissue.

In this paper we demonstrate a series of protocols for acquisition, analysis, and visualization of time-lapsed 3-D (x, y, z, t) images from within intact living cartilage (Fig. 1). First, we describe a data acquisition regimen that optimizes both signal-to-noise and cell viability. Second, we describe techniques to overcome the particular problems of accurate volume measurement within thick microscopical specimens. Physical interactions between the specimen and both the microscope illumination and fluorescence signal (Fig. 2) significantly affect the accuracy of the defined "confocal probe." The most important of these interactions are refractions that occur at all nonopaque boundaries through the optical path of both microscope and specimen, resulting in image blurring and distortion (3, 12, 21, 29, 32). In conjunction with confocal optical sectioning, these degradations give rise to fluorescence signal attenuation. The degree of sectioning depends on the objective numerical aperture (NA) and the imaging performance with a particular specimen. Low NA objectives provide longer working distance, but the finest sectioning is only possible with high NA. Long-working-distance objectives should, therefore, be calibrated for accurate measurements. Although the basic optics of the confocal microscope can be assessed, to obtain reliable measurements, the specimen must also be "calibrated." We present protocols for direct assessment of cartilage-induced attenuation and z-focus distortion in confocal microscopy. Third, we have extended conventional image analysis methods for measuring serial section data by combining 3-D visualization with calibrated volume measurements. Finally, we report the use of these new techniques by dynamically imaging living chondrocytes in situ and by demonstrating their volume regulatory behavior in response to osmotic manipulations.

MATERIALS AND METHODS

Tissue preparation and dye loading. Cartilage explants, obtained from the metacarpophalangeal joint of ~8-mo-old pigs, were taken from the trochlear ridge. Slices were cut longitudinally (20 × 5 × 5 mm) and suspended in *N*-2-hydroxyethylpiperazine-*N*′-2-ethanesulfonic acid (HEPES)-buffered Dulbecco's modified Eagle's medium (DMEM), and this initially provided a solution of 280 mosM (140 mM NaCl) at pH 7.4; hence it was not necessary to supply CO_2 during the course of the experiment (11, 34). Explants were positively labeled with 4.5 μM 5-chloromethylfluorescein diacetate (CMFDA; Molecular Probes, Eugene, OR) at 37°C for 15 min. The tissue was placed in the same orientation in a heated (37°C) perfusion chamber (15); this meant that we always knew which cartilage zone we were imaging. The chamber was mounted onto a modified MRC 600 CLSM (Bio-Rad Microscience, Hemel Hempstead, UK) (9), attached to a Diaphot inverted microscope (Nikon, Surrey, UK). All tissue experiments were carried out using a ×25, 0.8 NA Plan Neofluar objective lens with a variable correction collar for oil, glycerol, or water immersion (Carl Zeiss, Welwyn Garden City, UK).

Confocal microscopy. Quantitative fluorescence images were obtained by maintaining the eight-bit digitized signal between 20 and 235 gray levels (thus avoiding electronic saturation) and carefully controlling dye loading and laser intensity (avoiding fluorophore saturation). It was crucial to use the minimum laser intensity to maximize tissue viability, and our normal instrument setup resulted in 20 μW of laser illumination at the sample. Scanning speed and frame integration were optimized for image collection: 768 pixels (0.04 μm sampling) by 180 lines at 3 frames/s with a 2-frame integration. To maintain cell viability within the tissue explant, we optimized the imaging conditions using a sample perfusion medium containing propidium iodide (2).

Osmotic manipulation. A typical volume regulation experiment proceeded as follows: each cartilage explant was perfused with standard DMEM, and the initial 3-D fluorescence image of the series was acquired. The medium was replaced (over ~10 s) with a hypotonic solution (140 mosM,

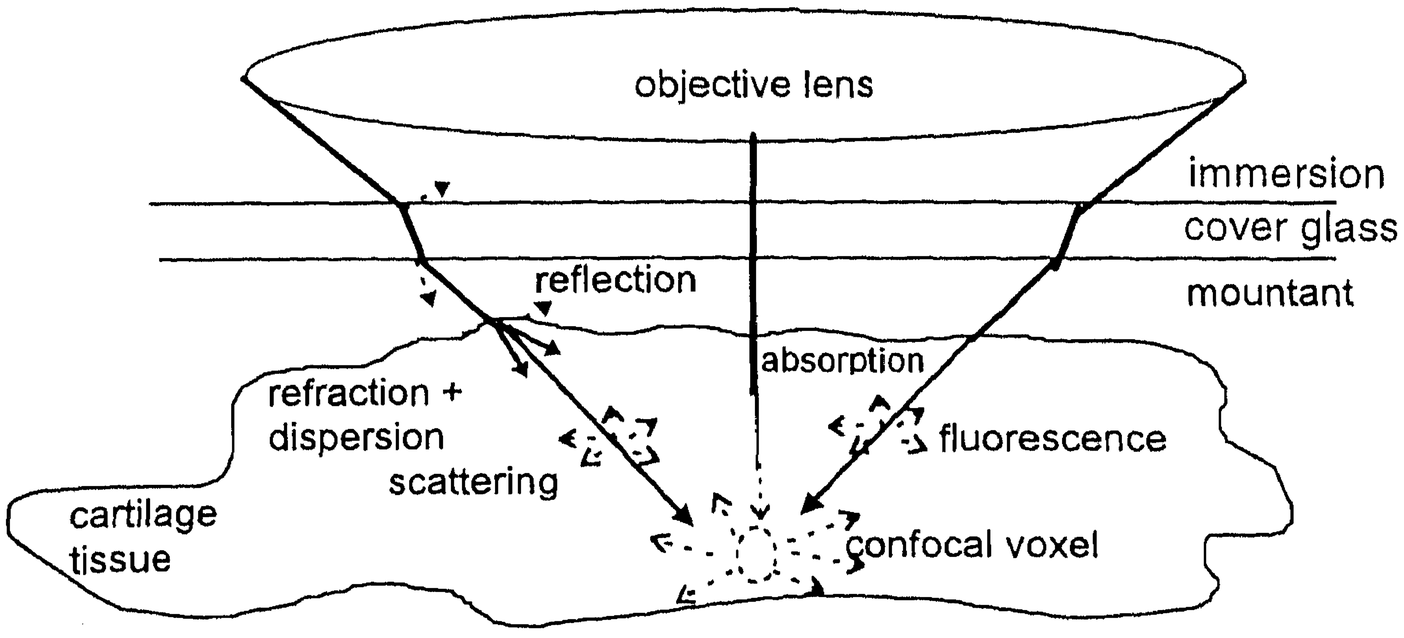

Fig. 2. Light interactions with cartilage. It is difficult to attribute the properties of the tissue to specific processes. Absorption depends on local and average concentrations of appropriate molecules as well as excitation and emission wavelengths. Absorption by fluorophore molecule is minimal. Refraction depends on refractive index for the particular material (cartilage consists of 80% water, with collagen and proteoglycan macromolecules), and wavelength-dependent dispersion is also different for many macromolecules. As a consequence of these processes, "confocal" voxels will be imaged with fidelity that is determined by composition and mounting environment of the cartilage, as well as the optical corrections of the microscope.

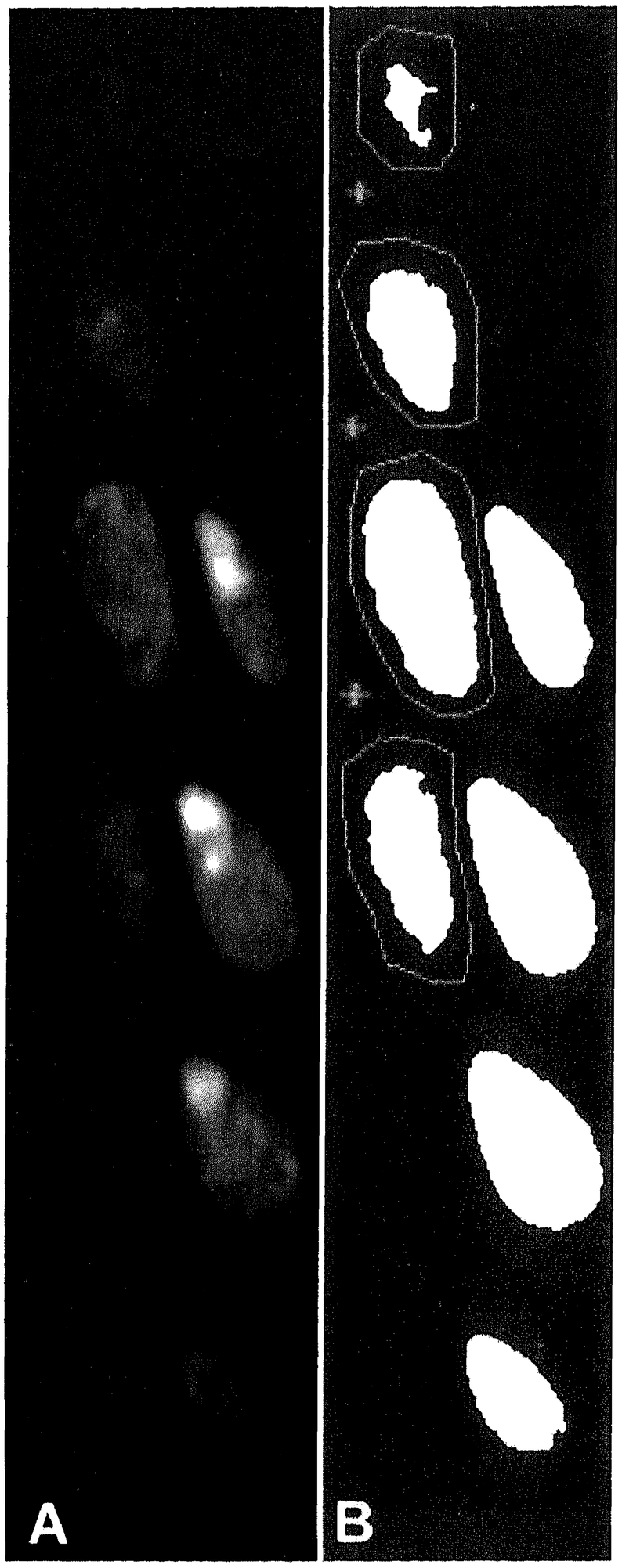

Fig. 3. Extraction of chondrocyte volume from summed optical sections. *A*: 6 optical slices, from the middle of a 3-dimensional (3-D) image containing 44 slices, through 2 adjacent chondrocytes in situ after labeling with 5-chloromethylfluorescein diacetate (CMFDA). *B*: slices were binarized using a single segmentation threshold at 50% (see text). All pixels with intensity equal to or above this threshold were defined as cell and set to 255. Pixels of intensity below this threshold were defined as extracellular matrix and set to 0. Subsequently, the areas of each binarized optical section were added together and multiplied by corrected z-increment to obtain cell volume.

pH 7.4), derived by diluting DMEM with water, and serial 3-D images were captured at 3- to 10-min intervals. At 15–20 min, the medium was replaced (over 10 s) with hypertonic DMEM (380 mosM, pH 7.4, 190 mM NaCl). 3-D images were then collected for up to 1 h. Typically, this particular experiment (N) was repeated three times, with fresh tissue and approximately five cells per time course (n).

Computer programs used for data acquisition and processing. All image data collection and manipulation were performed using the software packages COMOS, MPL, and Lasersharp (Bio-Rad Microscience) on a PC workstation. Graphs and trend-line analysis were carried out in Excel (Microsoft). Noise images were constructed in Semper (Synoptics).

Calibration of axial attenuation. The signal attenuation when focusing through aqueous fluorescent medium (the fluorescent sea response) (12, 32) was measured from two-dimensional (2-D) vertical (x, z) sections. Calibration data for the ×25 lens were collected using oil or water immersion into aqueous fluorescein (50 μM) and 488-nm excitation. Vertical sections were scanned with x sampling = 0.275 μm and z sampling = 0.4 μm.

Cartilage tissue was fixed in 4% paraformaldehyde and incubated in aqueous fluorescein for 48 h to ensure dye penetration. 2-D vertical sections were also collected through this tissue. This provided an estimate of the combined effects of sample absorption, refraction, and scattering (an in situ sea response). These calibration images were collected using either oil or water immersion.

Fluorescence attenuation profiles, along the z-axis, were extracted and parameterized (after normalization to the top of the sample) using a quadratic function. The parameterized

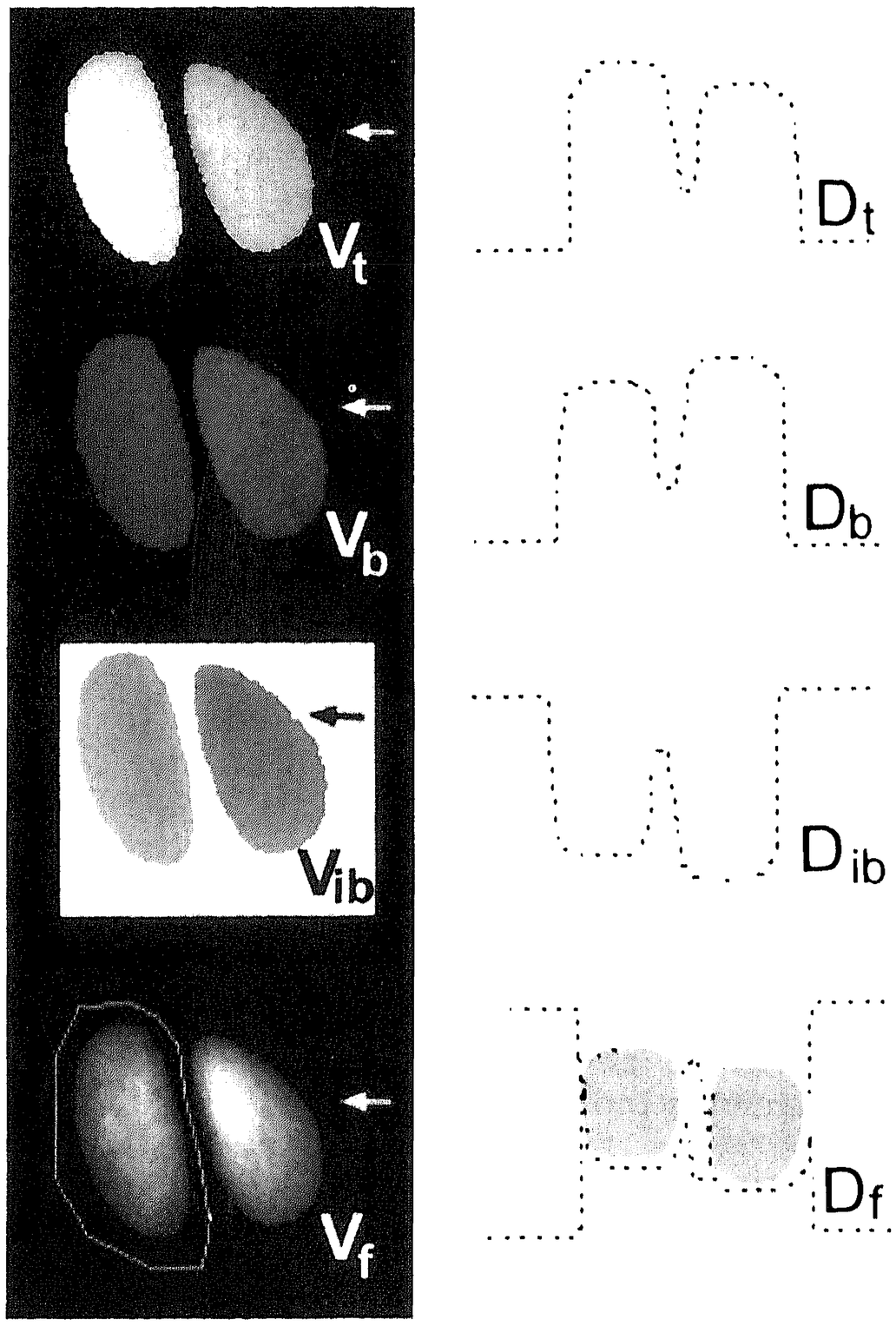

Fig. 4. Extraction of chondrocyte volume using surface reconstruction method. Cell boundary is displayed as a view (V) representing surface relief. Direct measurement of profile intensity across these views (in direction of arrow) gives 3-D coordinates of cell boundary (D). V_t, coordinate projection from top of cells; D_t, surface profile across top of cell; V_b, coordinate projection from below cells; D_b, surface profile from below cell; V_{ib}, same view as V_b with an inverted look-up table applied; D_{ib}, profile of lower surface as seen from above; V_f, final view representing cell thickness obtained by subtracting V_{ib} from V_t; D_f, diagram representing final result of subtracting D_{ib} from D_t. The volume is extracted by integrating all pixel values within the bounded volume.

axial attenuation function was subsequently used to correct each z-plane of 3-D fluorescence images collected during osmotic manipulations. This produced images with a spatial intensity transfer function that was nearly isotropic (32).

Calibration of z-focus distortion. To calibrate the distortion of axial focus due to mismatched immersion and mountant, we measured aqueous medium/glass boundary profiles in reflection and fluorescence through a "sandwich" of fluorescent buffer (53 μM) between cover glass and slide (12). The measured distance between the two inner glass/medium boundaries for particular immersion and mountant conditions was compared with the "correct" distance measured with a water-immersion lens.

A linear adjustment of the z-axis scaling was accomplished by *1*) applying a correction factor to the distance z-axis increment contained in the ".PIC" file format [particularly useful for accurate visualization of the 3-D (x, y, z) data] or *2*) directly applying the z-focus correction to the results of volume measurements whose values were linearly related to the z-calibration.

Finding the boundary of a cell in the digital image. To accurately measure the volume of positively labeled cells, an objective estimate of the cell boundary position was developed using solid fluorescent latex beads. The distribution of bead diameters [labeled as 7 ± 0.3 (SD) μm; Polysciences] was measured using a Coulter counter (model ZM; Electronics). 3-D images were obtained of the same beads immobilized on coverslips coated with 0.1% (wt/vol) poly-L-lysine.

We used the fluorescent calibration beads to empirically determine the boundary threshold (BT) as a percentage of the fluorescence maximum value. A 2-D projection of each bead image was made (MPL "maximum project" command) and binarized (MPL "lut", "contrast fix"). The diameters by confocal microscopy were compared with the distribution from Coulter counter analysis.

Calibration of the objective lens "confocality" for volume measurements. Chondrocytes were isolated from the tissue as described by Hall (11) for calibration experiments. Cells were positively labeled with CMFDA and allowed to adhere to a coverslip (before washing) and mounted in the observation chamber. 3-D images were collected with both the ×25 (low NA) and ×60 (high NA) objectives. Volumes were calculated and compared using protocols described below.

Volume measurement. Two different approaches have been developed to measure cell volume. First, each optical slice (Fig. 3*A*) was binarized, so that only the pixels above the BT are represented (Fig. 3*B*). The cross-sectional areas through the cell in each section were then summed and the total multiplied by the corrected z-increment to obtain the calibrated cell volume (in μm^3). The second method has been designed to compress the 3-D image into two 2-D views from which the volume and other well-defined morphological measurements can be made. The cell boundary was displayed as a view representing surface relief (Bio-Rad Thru-View) (31–33). Direct measurements of pixel position and values in these views give the 3-D (x, y, z) coordinates of the cell boundary; bright features were toward the viewer and the dimmer features were away. Cell volume was calculated from two such views (Fig. 4): from on top (V_t) and from below (V_b) the cell. From these views, a profile diagram across the cells showed the top surface (D_t) and bottom surface (D_b). When inverted (via a look-up table), the pixel values in V_b became a view of the cell underside from above [V_{ib}, and D_{ib} (in profile)]. A final view (V_f) representing the thickness of the cell (D_f) at each point was then V_t minus V_{ib}. The volume of any cell visible in this 3-D reconstruction was extracted by integrating all voxels within the bounded volume of the cell. The summed-area and reconstructed-height methods were compared, using 3-D confocal data of latex spheres immersed in a fluorescent glycerol medium.

Sensitivity of volume measurements to noise in fluorescence images. To assess the sensitivity of these techniques to noise, we estimated cell volumes from 3-D cartilage images after 16-frame averaging and with increasing levels of artificially added noise. Digital images with defined levels of shot noise (corresponding to instrumentation noise at low, medium, and high gain) were generated and added to the averaged fluorescence sections.

Visualization of dynamic changes in cell volume. 3-D intensity reconstructions were made at each time point of the 4-D image sequence collected during osmotic manipulations. The brightness in these reconstructions represented fluorescence intensity, and color was used to code the relative volume of each cell with respect to the initial volume at the start of the experiment. This was achieved by extracting each cell from a 3-D time point and measuring the volume before generating its 3-D reconstruction. The corresponding height image for all cells was also generated and used to merge each volume-coded (colored) reconstruction into the final view. In this view ("looking into" the cartilage), cells deeper into the original (transparent) tissue sample were "realistically" obscured by overlying cells.

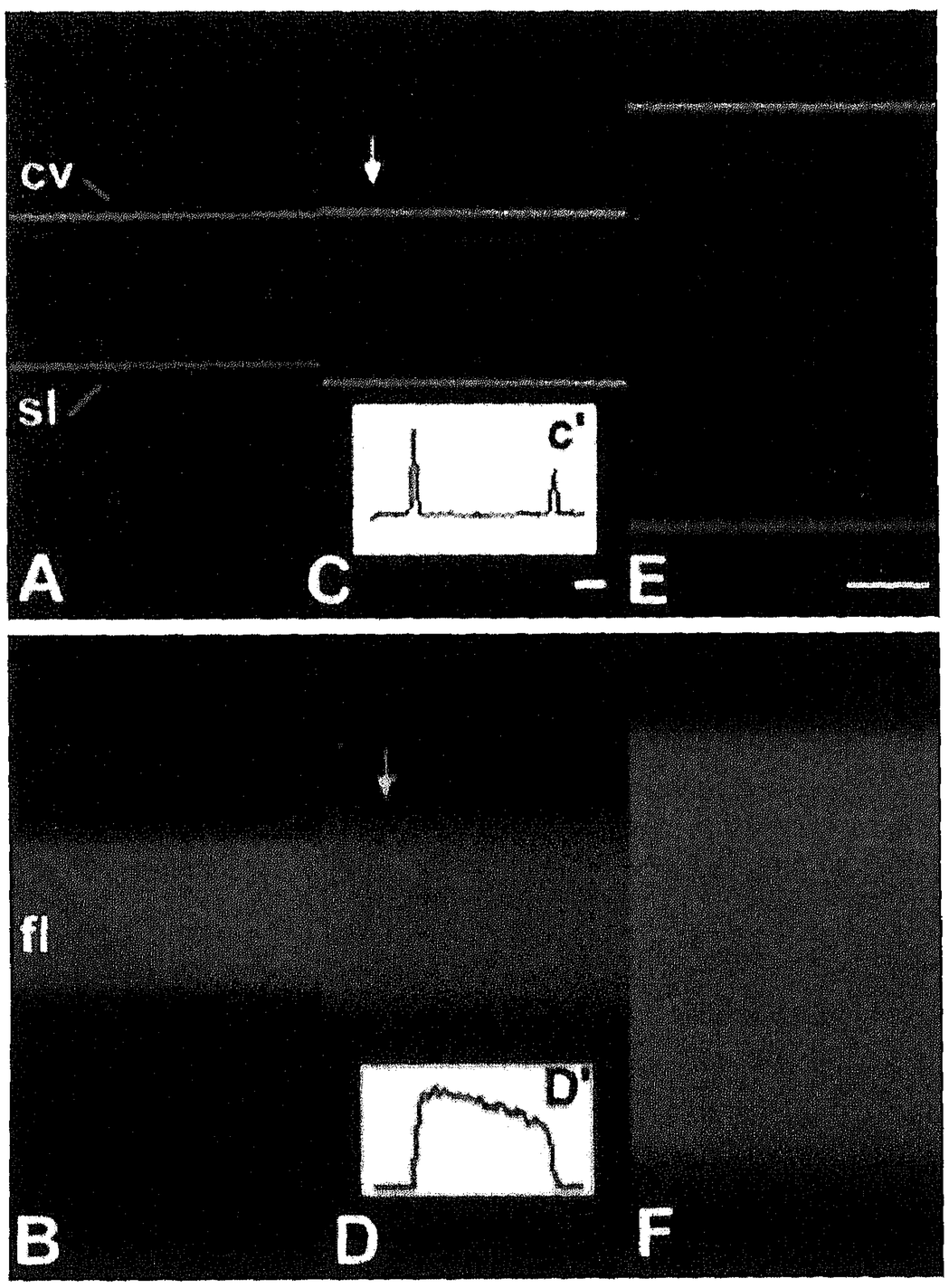

Fig. 5. Reflection and fluorescence profiles through a sandwich of fluorescent buffer (fl) between a cover glass (cv) and slide (sl). *A*: reflection profile collected with the ×25 lens in water-immersion mode. *B*: corresponding fluorescence profile. *C*: reflection profile collected with the ×25 lens in oil-immersion mode. *C' inset*: graph of typical reflection intensity across glass/buffer interfaces (in direction of arrow). *D*: corresponding fluorescence profile. *D' inset*: typical graph of fluorescence intensity across glass/buffer interfaces through fluorescent buffer. *E*: reflection profile collected with ×60 oil-immersion lens. *F*: corresponding fluorescence profile. Bars = 10 μm.

RESULTS

Calibration of z-focus distortion. Calibration of the spatial z-correction factor was obtained from vertical (x, z) confocal reflection sections across glass/aqueous medium/glass boundaries (Fig. 5, *A–F*) using the ×25 multi-immersion objective. The apparent glass-to-glass distance using different collecting conditions was used together with "true" z-distance, defined using water immersion (Fig. 5*A*) to calibrate the distorted z-distances (e.g., with oil immersion; Fig. 5*C*). Oil immersion into aqueous medium resulted in a z-distance that was 14% greater than the true distance using water immersion. Hence the ratio of distorted to true z-focus, the focus-correction factor for this lens with oil immersion, was 0.88. The focus correction obtained for an oil-immersion ×60, 1.4 NA lens (Fig. 5*E*) was 0.83. These results were subsequently applied to data collected from aqueous mounted samples using the corresponding objectives.

Calibration of axial attenuation. Signal attenuation was measured from vertical (x, z) sections through aqueous fluorescein between cover glass and slide and also through fluorescein-permeated cartilage. The water immersion ×25 lens showed no appreciable attenuation with depth (Fig. 6*A*), whereas the same lens in oil-immersion mode demonstrated an intensity increase to 120% over 80 μm (Fig. 6*B*). However, the ×60 oil objective showed moderate attenuation to 60% over 60 μm. A fitted quadratic trend line to the axial intensity profile with the ×60 objective is shown in Fig. 6*C*. Attenuation curves were derived from in situ sea responses for the same lens and immersion conditions as the sea responses. The corresponding curve and fitted quadratic parameters are shown in Fig. 6, *D–F*. In contrast to the sea response, the 0.8 NA lens showed a significant attenuation when focusing into tissue for all immersion conditions. At a nominal focus of 60 μm into the tissue, the relative intensity was attenuated to 33% for oil immersion and to 25% for water, clearly showing reduced signal loss with oil immersion into cartilage. As expected, the 1.4 NA plan-apo lens gave severe attenuation with depth into the tissue, and only 5% of the signal remained at 60 μm.

Geometric and photometric correction of cartilage images. Confocal 2-D (x, z) sections together with reconstructions of porcine chondrocytes (Fig. 7, *A–F*) illustrate the application of the parameterized corrections to experimental data collected with the ×25, 0.8 NA lens. The original or "raw" data (Fig. 7*A*) showed an axial reduction in intensity within the vertical sections. Additionally, these images were "stretched out" axially. These same data were geometrically corrected by an

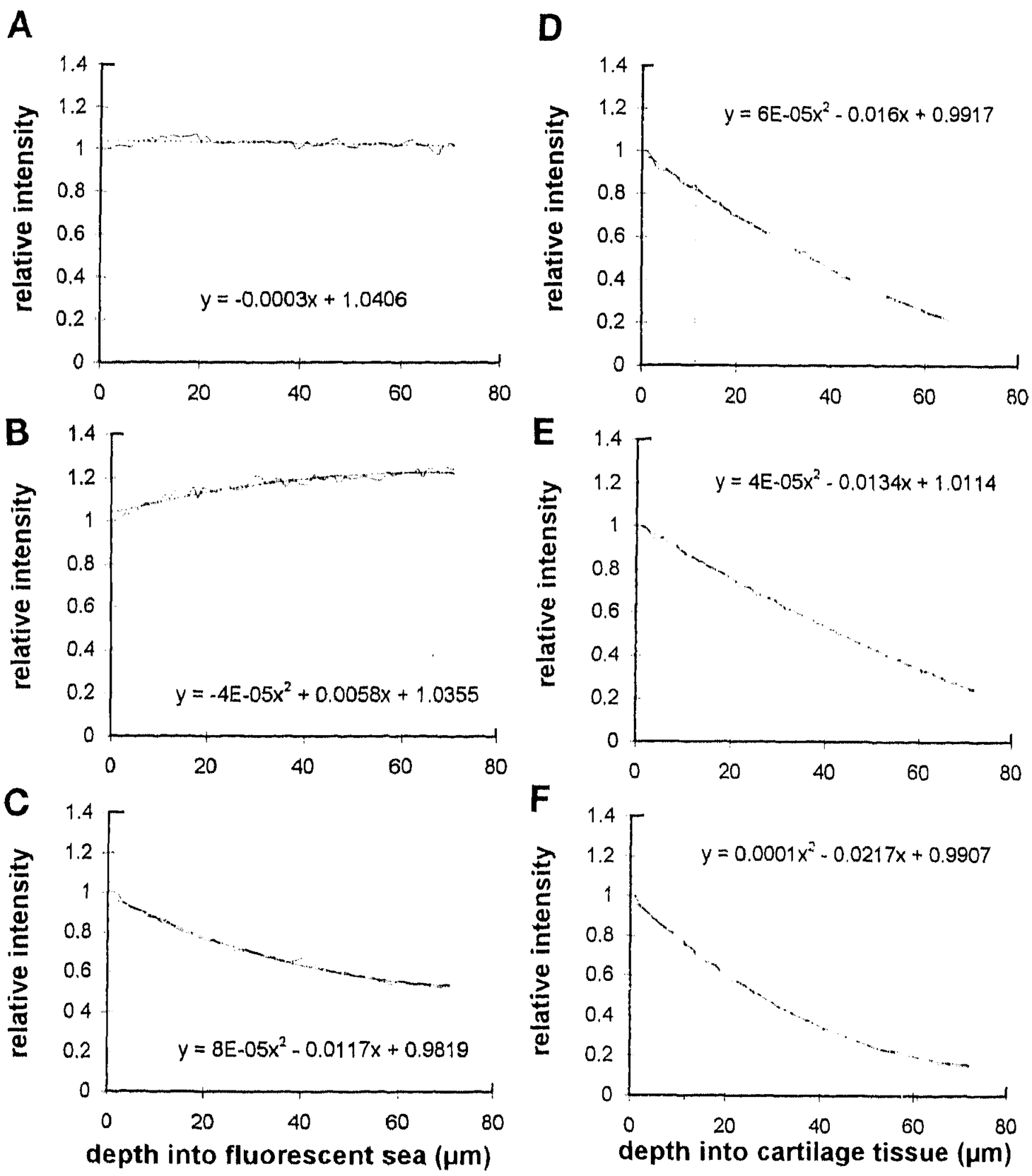

Fig. 6. Fluorescence intensity profiles measured from the cover glass into a fluorescein solution (*A–C*) or cartilage bathed in aqueous fluorescein (*D–F*). Each intensity profile was fitted with a quadratic trend line, and the equation is shown in the relevant panel. E, exponential (base 10). Vertical lines indicate regions used for all image collection (15–60 μm). Profile of relative intensity attenuation through a fluorescein sea obtained with ×25 objective in water-immersion mode (*A*) or in oil-immersion mode (*B*). *C*: relative intensity attenuation through fluorescein sea obtained with ×60 oil objective. Relative intensity attenuation through fluorescein-pregnated cartilage tissue obtained with ×25 objective in water-immersion mode (*D*) or oil-immersion mode (*E*). *F*: relative intensity attenuation through fluorescein-pregnated cartilage tissue obtained with ×60 oil objective.

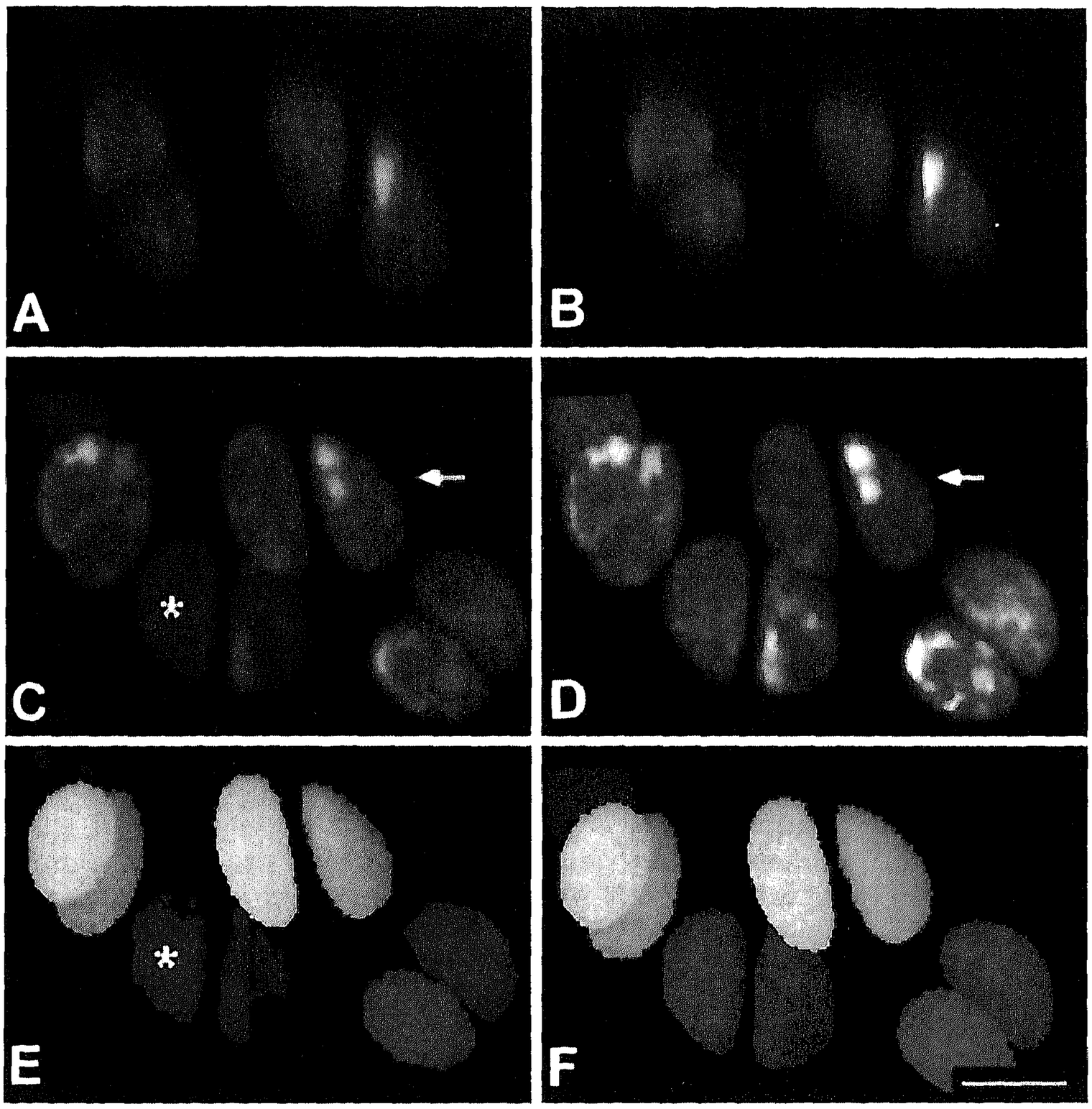

Fig. 7. Postacquisition digital correction of axial z-distortion and attenuation in cartilage tissue. *A*: vertical (x, z) sections through uncorrected data at positions indicated by arrows in *C* and *D*, illustrating significant axial attenuation and stretching out. *B*: same vertical section after geometric correction of both the axial focus, using a factor of 0.88, and the axial signal attenuation, using the parameterized correction functions. *C*: maximum intensity reconstruction of uncorrected data. Cell deepest into the tissue (asterisk) "appears" to exhibit less fluorescence than cells at surface. *D*: maximum intensity reconstruction of corrected data. Relative fluorescence intensity of cells is now homogenous. *E*: 3-D surface reconstruction of uncorrected data using a 50% segmentation threshold obtained from cells closer to the tissue edge. Cells deep in the tissue become degraded (asterisk). *F*: 3-D surface reconstruction of corrected data using same segmentation threshold as *E*. All cells are now included, and hence more morphological information is available. Bars = 10 μm.

axial factor of 0.88, and fluorescence intensities were divided by corresponding factors from our axial attenuation function (Fig. 7*B*). Reconstructions of the 3-D serial-section image into a single 2-D view demonstrated the benefits of appropriate corrections. A maximum-intensity projection of the uncorrected data showed that cells located deeper in the tissue (Fig. 7*C*, asterisk) were dimmer than cells at the tissue surface (arrow). To ascertain whether such an apparent distribution is physiologically relevant (e.g., whether these cells contain less fluorescent probe, etc.), the images must be corrected for attenuation. Application of the intensity correction (Fig. 7*D*) showed that the probe distribution in the cell population is independent of z-depth. Visualization of both the uncorrected (Fig. 7*E*) and corrected (Fig. 7*F*) data, using a simple coordinate reconstruction, also revealed the importance of the correction protocols. The height-coded algorithm used a single-intensity threshold to segment cells from the matrix throughout the entire 3-D image. A view is produced, giving x, y, z coordinates representing the visible surface of each cell. With uncorrected 3-D images, a threshold suitable for the cells at the tissue surface assigned deeper cells within the tissue with artificially reduced dimensions (Fig. 7*E*, asterisk) and vice versa. Therefore, to efficiently represent all of the morphological information throughout the entire 3-D image (Fig. 7*F*), sample-specific corrections must be applied.

Segmentation: objective determination of the cell boundary. We have used two methods to define the BT. The first was independent of axial aberrations. We ran a sample of fluorescent latex beads through a Coulter counter to obtain the distribution of diameters (Fig. 8*A*). The modal value from this distribution was 6.64 μm. From the same sample we obtained 3-D images of immobilized beads (n = 100). An estimate of the sphere diameter was derived as described in MATERIALS AND METHODS. Using a cell-segmentation threshold of 50% (Fig. 8*B*), we obtained from images a distribution of diameters that correlates closely to that obtained with the Coulter counter (mode = 6.6 μm). The second method employed the additional information from the reflection and fluorescence medium/glass profiles used for measuring z-focus distortion [Fig. 5, *C′* and *D′* (*insets*)]. We measured the distance between the two reflection peaks and also between the 50% fluorescence points. The ratio of reflection z-distance to fluorescence z-distance was 1.006, indicating that the segmentation at a 50% threshold provided an accurate estimate of the distance. An intensity profile across the chondrocyte boundary (Fig. 8*C*) demonstrated the procedure for obtaining the BT for a cell. The low-intensity region represented the extracellular matrix and the bright region represented the cell (i.e., intracellular) fluorescence. Across the boundary the intensity changed smoothly between these two extremes, with a profile dependent on the cell size and shape and the imaging

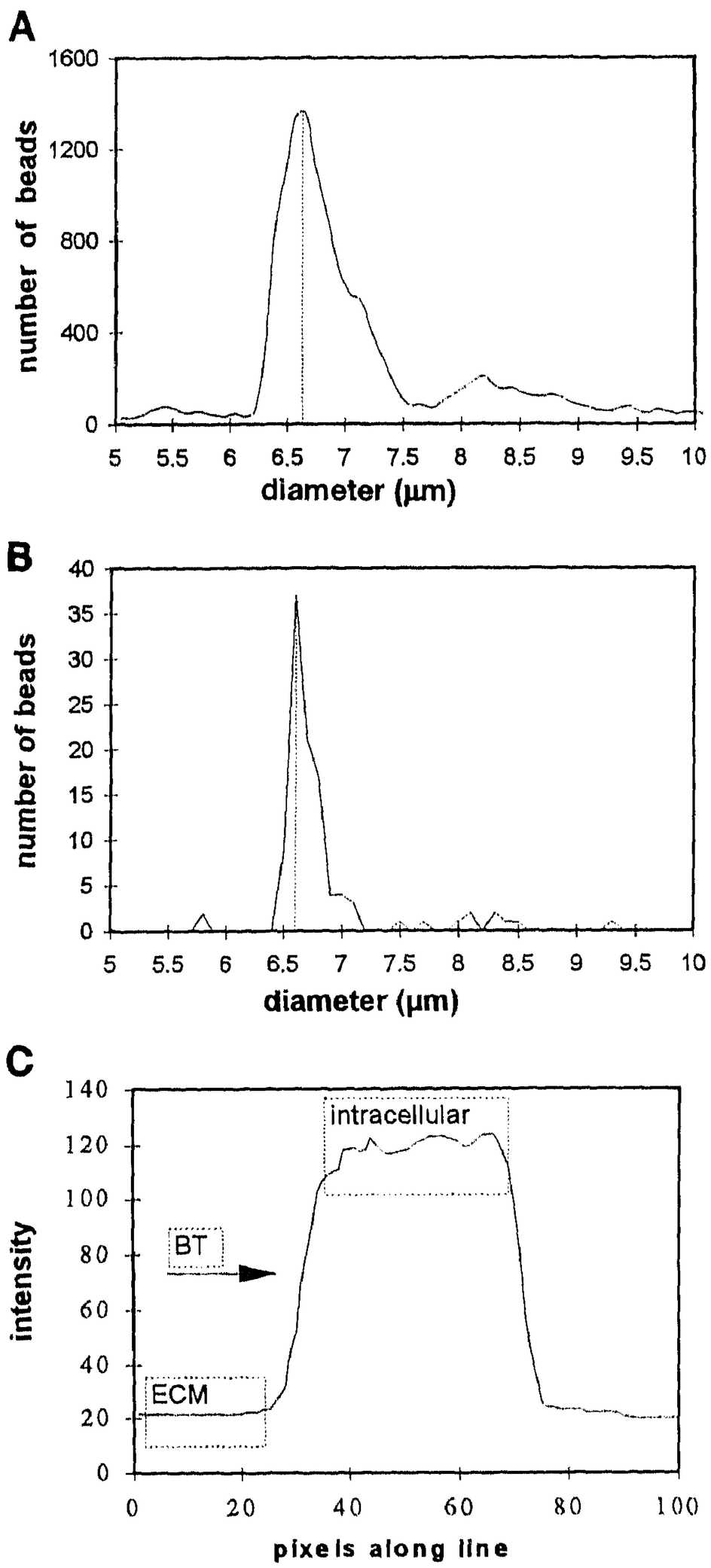

Fig. 8. Defining the segmentation threshold. *A*: distribution of fluorescent bead diameters from Coulter counter measurements assuming spherical symmetry. *B*: distribution of fluorescent bead diameters from *x*, *y* maximum reconstructions of 3-D images. Diameters were calculated from the area, assuming radial symmetry. Boundary segmentation threshold was as defined as 50% of maximum intensity minus the background. Mode = 6.6 µm. *C*: intensity profile across a CMFDA-labeled chondrocyte. Highest intensities represent intracellular milieu, whereas lowest intensities represent extracellular matrix (ECM). Halfway between these 2 extremes has been taken to define the cell boundary. This 50% value was termed the boundary threshold (BT).

properties of the microscope. Following our calibrations (described in the previous section, *Geometric and photometric correction of cartilage images),* BT was defined as the point where the intensity fell to halfway (50%) between the average minimum (I_{min}) and maximum (I_{max}) values (Fig. 8*C*, arrow). The variation of BT with image noise and dye compartmentalization was accounted for by determining confidence limits based on

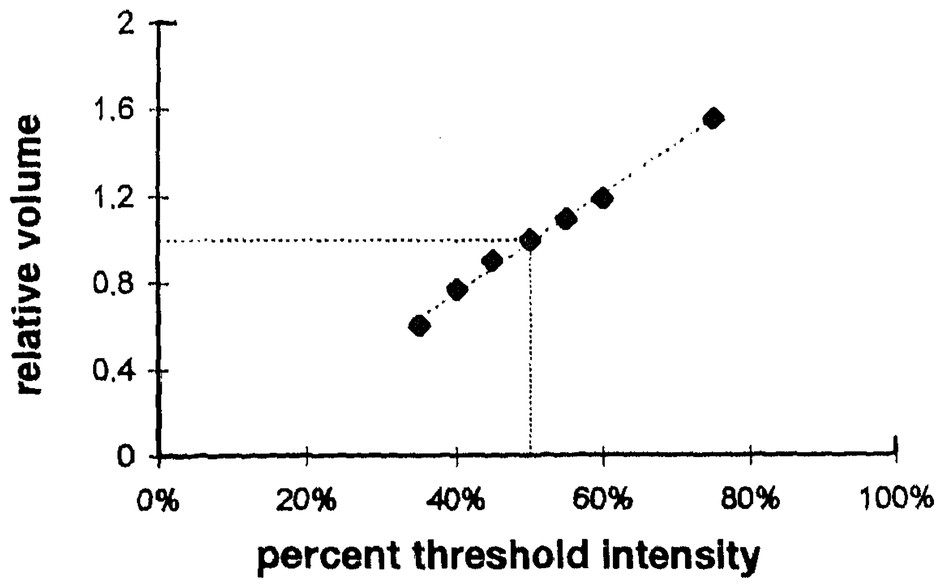

Fig. 9. Variation in relative cell volume derived from different percent segmentation thresholds (compared with 50%). The relationship is such that a 1% error in determining the boundary results in a 2% error in the extracted volume.

two additional threshold values derived from the average maximum value ± SD (I_{std}). The method thus estimated three separate volumes for each cell derived from the following BT formulas

$$(I_{min} + I_{max})/2 \quad (1)$$

$$(I_{min} + I_{max} + I_{std})/2 \quad (2)$$

$$(I_{min} + I_{max} - I_{std})/2 \quad (3)$$

Formulas 1 and *2* enabled us to define the volume limits and hence attribute confidence to the BT-derived volume derived in *formula 1*. The BT segmentation value (defining the cell membrane within 3-D confocal images) profoundly affected the apparent volume of a cell (Fig. 9). The variation in relative volume (compared with the correct 50% volume, checked against Coulter counter measurements) with varying BT values showed that a 1% error in BT gave a 2% error in volume.

Calibration of objective lens confocality. To accurately calibrate volumes imaged by high and low NA objectives, against a well-characterized conventional method using identical specimens, we determined volumes of isolated chondrocytes by confocal microscopy and with

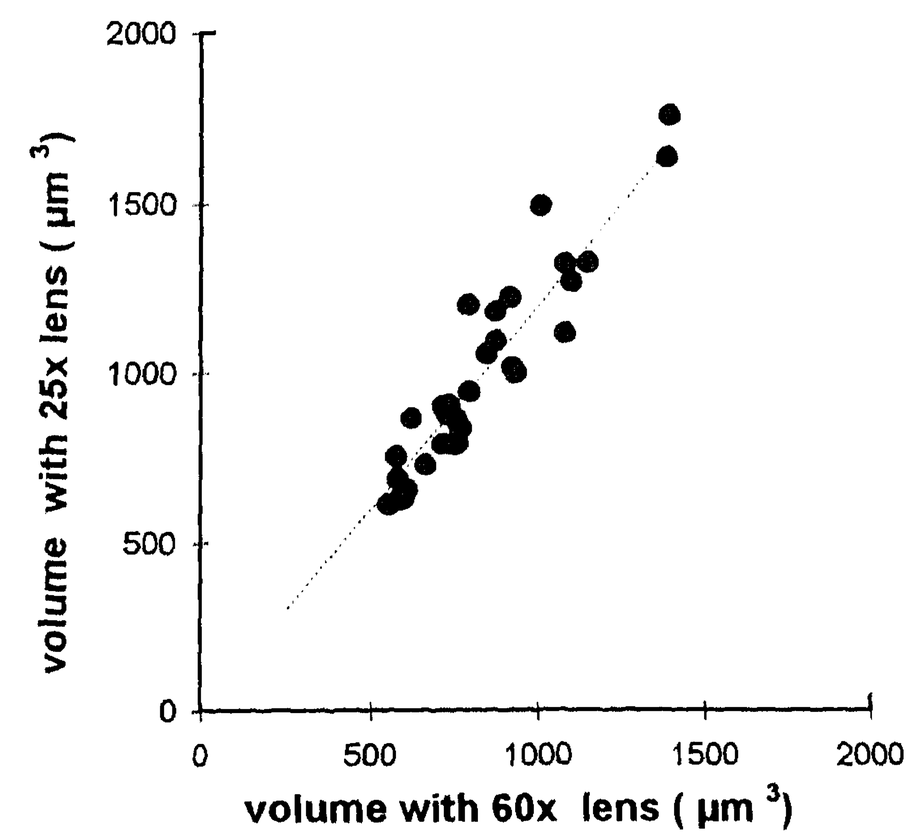

Fig. 10. Scatter plot comparison of isolated chondrocyte volumes measured using ×60 objective lens and ×25 objective lens. Data are fitted with a linear trend line, having a correlation coefficient of 0.87 and a slope of 1.21.

Table 1. *Effect of high-frequency noise on volume measurements*

Shot noise (per pixel)	0	0.001	0.005	0.010
Relative volume	1	0.99	0.96	0.8
Relative volume limits	±0.03	±0.07	±0.34	±0.47

Relative volume limits are ±SD; $n = 15$ cells.

a Coulter counter. Chondrocytes were isolated and loaded with CMFDA (as described in MATERIALS AND METHODS). CLSM volumes were determined for the ×25, 0.8 NA objective and the ×60, 1.4 NA objective. The lower NA lens consistently gave volumes 20% larger than those obtained with the higher NA lens (Fig. 10). We compared the CLSM volumes of isolated cells (collected with the ×60 lens) with Coulter counter estimation of a sample from an isolated cell suspension in the same conditions (11). Significantly, if we assumed the cells were spherical and estimated the volumes using only diameter measurements (from *x*, *y* projections), similar volume measurements were obtained from both ×25 and ×60 lenses. Therefore, the difference in volumes with these objectives arose entirely from *z*-dependent imaging distortions. When measuring cellular volumes deep within the tissue, we were restricted to using the ×25 lens that provided a long working distance. We could, therefore, monitor cells well away from the cut surface (at least 15 μm farther into the tissue). The lower NA of the ×25 lens resulted in reduced confocality, artificially inflating the measured volumes along the *z*-axis. The high NA objective provided optimum confocality for calibration with isolated cells but gave severe attenuation when imaging into cartilage tissue. We applied a further confocality correction factor of 0.81 to volumes derived from images collected with the ×25 lens.

Effect of image noise on volume measurements. The signal-to-noise quality of the 3-D image played a crucial role in the accuracy of volume measurements. To test the effect of image noise empirically, we collected 3-D images of chondrocytes in situ after labeling with

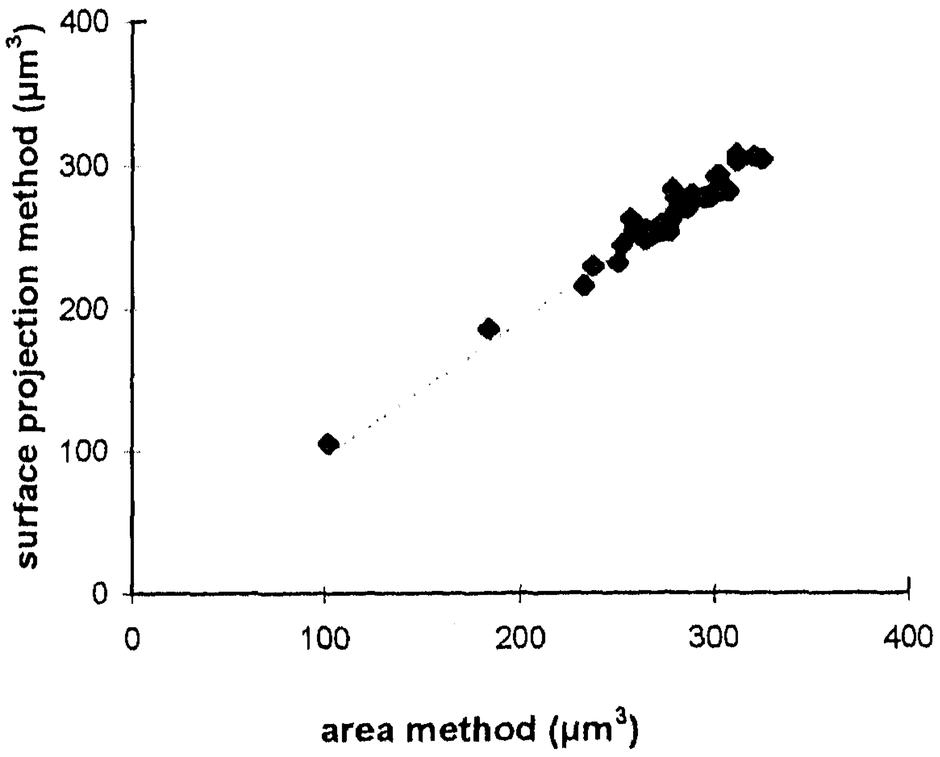

Fig. 11. Scatter plot to compare area summation and surface reconstruction methods to extract volume measurements. Data are fitted with a linear trend line, having a correlation coefficient of 0.95 and slope of 0.96.

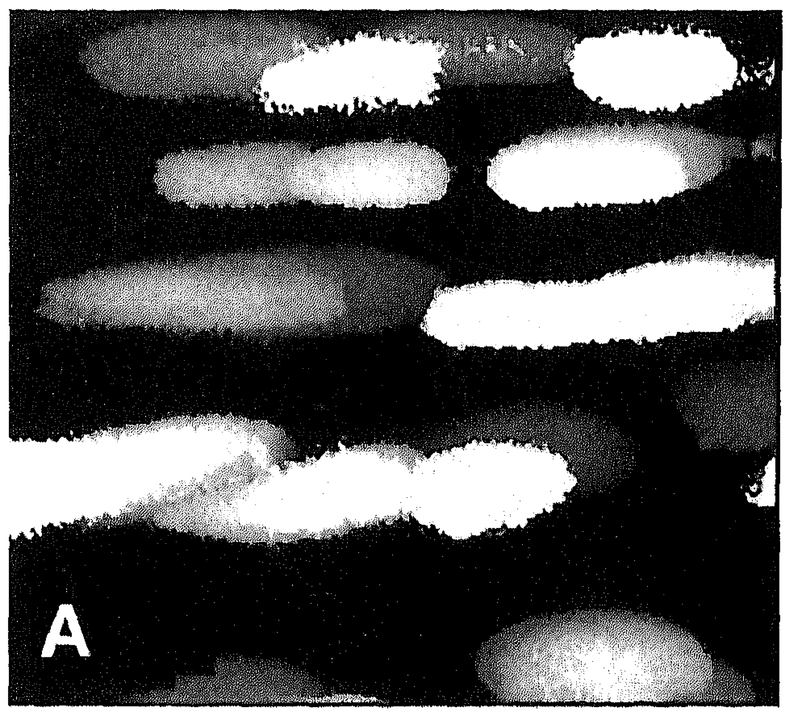

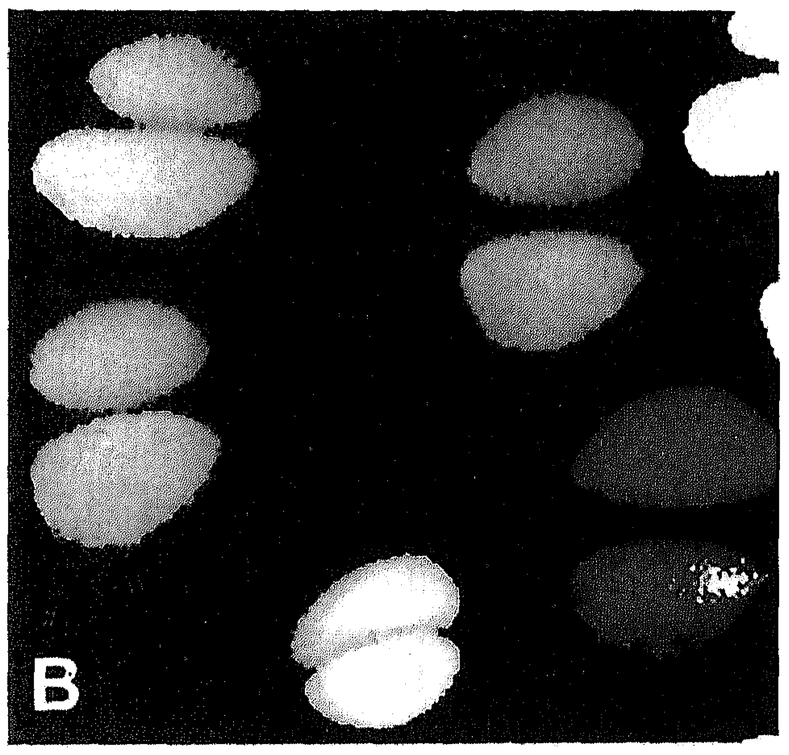

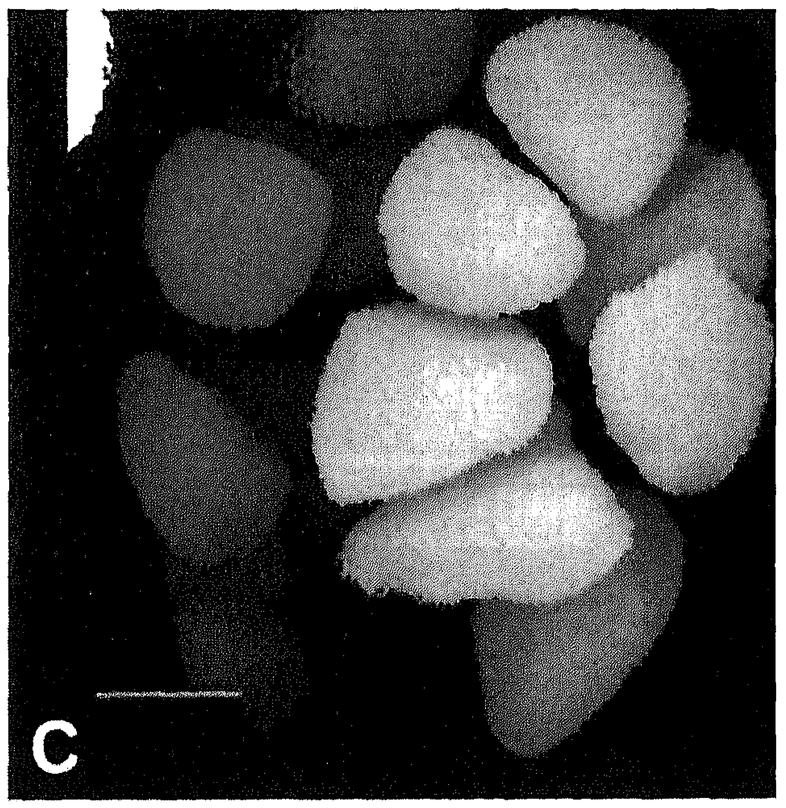

Fig. 12. 3-D surface reconstructions of porcine cartilage chondrocytes in different zones: cells within the surface region (*A*), the midzone (*B*), and the deep zone (*C*). Images clearly show that cell shape and arrangement vary significantly, forming distinct populations. Bar = 10 μm.

CMFDA, with 16-frame averaging and 3 × 3 median filtering of each section. We extracted cell volumes from these noise-free images for a BT of 50% and also for BT values of 50 ± 1% (SD). This gave confidence limits for "50% volumes." We repeated these three estimations after digitally adding one of three levels of random noise (corresponding to low, medium, and high gain on

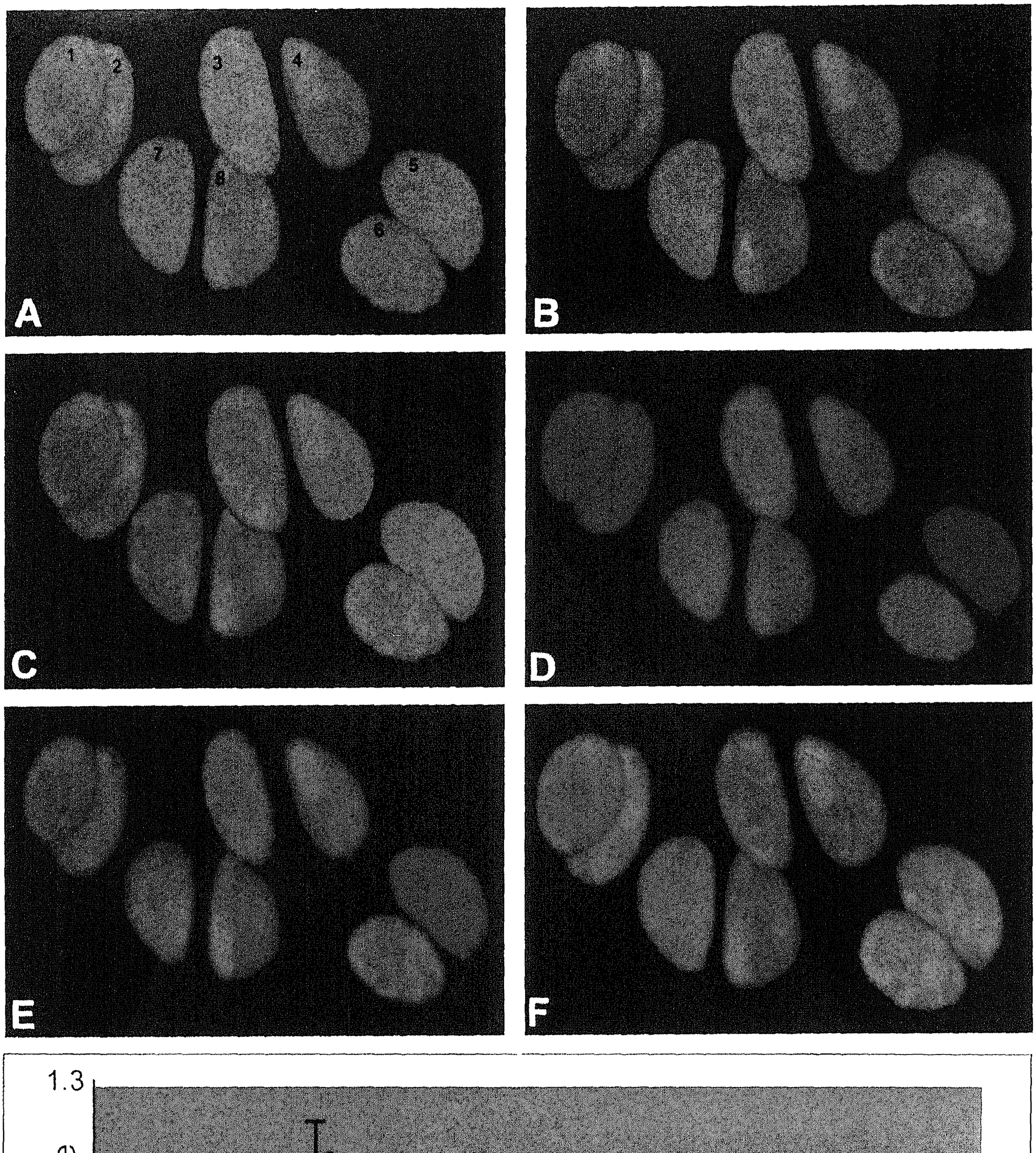
1
2
3
4
5
6
7
8
A
B
C
D
E
F
1.3
mean relative volume
0.55
0
time (mins)
60
G

Table 2. *Zonal variation in chondrocyte volume measurement in situ using CLSM*

Zone	Volume, μm^3
Surface	512 ± 96
Mid	665 ± 210
Deep	703 ± 200

Values are means ± SD; $n > 50$ cells in each zone, taken from at least 3 different tissue slices. CLSM, confocal laser-scanning microscopy.

the CLSM detector circuits). The results (Table 1) showed that the effect on the measured 50% volume was not significant for low or medium gain, but at high gain the extracted volume decreased to 0.8 times the 50% volume derived from the noise-free image. However, confidence limits [BT = 50 ± 1 (SD)] were affected significantly by all levels of added noise, and this value confined the acceptable noise tolerance. Because we were interested in measuring the dynamic physiological volume responses in the face of osmotic perturbation, we optimized our imaging protocols (as described in MATERIALS AND METHODS) to maintain the SD of volume measurements to within ±7%, corresponding to low detector gain.

Volume measurements of in situ chondrocytes. A comparison of the summed-area and height-reconstruction methods for measuring cell volume shows that, for well-segmented cells and with appropriate image corrections, the correlation coefficient was 0.95 (Fig. 11). Subsequently, the faster reconstruction method was used to map chondrocyte shape (Fig. 12, *A–C*) and volume (Table 2) in the tissue. Cells in the surface zone were elongated and oriented parallel to the tissue edge (Fig. 12*A*). The midzone region consisted of cells not so densely packed and hemispherical in shape (Fig. 12*B*). They were usually arranged in "doublets" orientated perpendicular to the tissue edge. In the deep zone toward the bone, usually six to nine cells were grouped together (Fig. 12*C*). The mean volume of chondrocytes increased from the surface toward the deeper zone (Table 2).

Dynamic changes of cell volume. A key objective of this work is to apply these new methods of determining dynamic changes in chondrocyte volume in situ to follow changes in response to osmotic perturbations. Figure 13 shows the results of a typical time course experiment following cell volume changes during exposure of porcine chondrocytes in situ to anisotonic conditions, in particular, cell volume recovery in response to hypertonic shrinking after preswelling. The montage shows changes in relative cell volume (Fig. 13*G*) and corresponding reconstructions of 3-D confocal images at six time points (Fig. 13, *A–F*). These novel reconstructions visualize the chondrocyte morphology at the same time as indicating the relative changes in cell volume (coded in color) with respect to their initial volume at time point zero (green). On addition of a hypotonic shock (280–140 mosM), the cells enlarged by varying amounts, ranging between 10 and 30% (e.g., changing from green toward red). In this data set, the chondrocyte doublet furthest into the tissue showed a delayed response but enlarged to the greatest extent. The cells were then exposed to a hypertonic challenge (380 mosM); all cells shrank dramatically to ~60% of their initial volume (visualized as shades of blue). Cells subsequently exhibited volume regulation returning toward their original volume (e.g., from blue back toward green); the initial recovery rate for the time course presented in Fig. 13 ($n = 8$) varied from 1.8%/min (i.e., *cell 3*, remaining blue in Fig. 13*E*) to 4.5%/min (i.e., *cell 8*, significantly more green in Fig. 13*E*), with the cells achieving a mean recovery of 92 ± 9% (SD) after 12 min. A final time point was collected 40 min after the start of the shrinking phase to ensure that the cells remained viable after accomplishing volume recovery. With the use of this experimental regime, the cells always responded in a similar manner; however, the extent of response varied from slice to slice. Combining the results from three time courses [i.e., different tissue slices from different animal joints (slices = 3, cells = 14)], on average the cells increased their volume by 20 ± 9% and shrank by 29 ± 10% in response to a hypertonic shock, and the corresponding mean recovery rate was 4.1 ± 1.8%/min to a restored mean relative volume of 94.6 ± 11%.

DISCUSSION

In this paper we have described new protocols to acquire, visualize, and measure the dynamic volumes of chondrocytes in situ during imposed changes in the osmotic environment. Other workers have used tissue histological methods combined with physical sectioning and stereological estimators to determine chondrocyte volume and morphology (7, 20). However, this approach necessitates the dehydration of tissue during preparation, which causes membrane distortions and cell shrinkage. Also, it prohibits the study of dynamic volume responses, which forms a key component of our

Fig. 13. Chondrocytes in situ undergoing post-regulatory volume decrease/regulatory volume increase mechanisms in response to appropriate osmotic stimuli. 3-D images were obtained through 4 doublets (8 cells) labeled with CMFDA at different time points before, during, and after exposure to anisotonic conditions. Appropriate reconstructions were made of each image to produce views represented in *A–F*. Absolute and subsequently relative volumes of each cell at each time point were also extracted, and this parameter is represented by color. Original time point encodes all cells green, since their relative volume is 1.0 (*A*). These cells were then exposed to a hypotonic stimulus (perfusion bath changed from 280 to 140 mosM). Cells swell to different extents (color tends toward red; *B* and *C*). After this preswelling, cells were exposed to a hypertonic perturbation (perfusion bath changed from 140 to 380 mosM). All cells shrink coordinately (become blue; *D*) and recover their volume at different rates (color changes toward green; *E* and *F*). *G*: graphical representation of events plots mean relative volume ± 1 SD against time. Graph overlays contrast wedge so that observer can follow actual numerical changes as well as color changes and relate these to individual cells in previous panels.

investigation. This paper has both strengthened and expanded previous work that used confocal microscopy to determine the volume of living cells (4, 10, 24, 32). Our integrated protocol, consisting of fully optimized individual steps, simultaneously encompasses three major aims: *1*) obtaining 4-D images at satisfactory noise levels, *2*) precision estimation of fluorescence intensity and volume, and *3*) maintaining the viability (physiological status) of the chondrocyte in the tissue.

We have demonstrated the importance of considering cartilage as an optical component of the imaging system. Significant spherical aberration due to refractive index mismatch in the system results in axial distortion of the focal position. Good agreement was found between the measured focus error in glass/medium reflection profiles and the *z*-correction factor (0.82) previously described for a high NA (1.4) ×60 oil immersion into aqueous samples (12, 32). The larger axial distortion correction (0.88) obtained with the ×25, 0.8 NA objective is indicative of the fact that the confocality of this lens is not optimal (32). However, this is similar to the focus error reported by some workers who obtained a *z*-correction of 0.87 with a ×60, 1.4 NA objective lens (10) using a partially confocal slit detection instrument (25). These results, taken together, show that in confocal imaging the principal spatial distortion of axial focus is due to the optical features of the sample.

Although the *z*-focus error seems to be slightly dependent on the objective NA, attenuation is significantly dependent on NA, following directly from the combination of *z*-discrimination and refraction-induced aberrations. Previous papers have described these attenuation effects when focusing into an optically mismatched medium (3, 12, 21, 32). This study discusses an empirical approach to compensating for the axial attenuation, taking into account the unique properties of articular cartilage. A thick cartilage sample was infiltrated with a homogeneous distribution of a small fluorescent molecule. In all cases the axial intensity profiles were best characterized by a quadratic model; the quadratic, linear, and constant terms in this parametric description of attenuation directly relate to the amount of blurring from the specific optical properties of this tissue (32).

Time-lapsed 3-D images present unique problems for data analysis and visualization, and conventional tools were found inappropriate for the task (5, 31). First, we wanted to be able to compress each 3-D image of the sequence (i.e., each time point) into a single quantitative view from which cell volume could be extracted, without referring back to the optical slices. In contrast to other volume display methods (5, 10) derived from computer modeling, our method generates a quantitative coordinate or thickness view representing the entire cell. This approach combines, for the first time, the ability to simultaneously visualize and measure cell volume in a single view. We have also devised a second type of 4-D reconstruction that uses color to represent relative changes in cell volume, hence contrasting individual and population volume responses, while retaining a view of the cell morphology.

We have demonstrated that the technique of confocal microscopy and vital cell labeling both combine to provide a powerful tool for the direct observation of volume behavior during experimental manipulation. The major advantage of our method is that it enables determination of absolute cell volumes. In agreement with previous reports, we show a trend of increasing volume with tissue depth (7); however, to date there are insufficient data in the literature to compare results from equivalent ages and species.

We have found particular similarities between some aspects of our protocol and that described by Guilak (10). Our calibration paradigm is similar, but we have more accurately determined the fluorescence attenuation to be quadratic in nature, over a greater distance into the cartilage than the previously reported linear approximation for the first 35 μm. This allows more accurate measurements, deeper into the tissue, complimenting our improved volume calibration against Coulter counter methods. A more substantial difference is the extension in our study to multiple time points and dynamic (4-D) volume imaging. To ensure the success of this approach in living cartilage, we have optimized the 4-D data collection protocols for noise tolerance, dye loading, and rapid imaging. The added temporal nature of our results has required a new visualization method that simultaneously displays cell distribution and morphology together with individual cell volumes, relative to the start of the experiment. This makes use of novel voxel intensity-based reconstruction in combination with 24-bit true color for maximum use of display resources, in contrast to the object-based geometric surface modeling employed by Guilak (10). We do not, at present, measure cell surface area or determine related morphological parameters, although these measures can be derived from our coordinate reconstructions.

One important conclusion from the present work is that exposure of cartilage explants to solutions of different osmolarity causes changes to chondrocyte volume. Thus decreasing osmotic pressure causes rapid cell swelling that is rather surprising, given the nature of cartilage matrix, which is macroscopically rigid. When exposed to hypotonic solutions, the swelling of some cells deep within the tissue appears to lag behind swelling of cells nearer the surface. This might be expected due to limiting diffusion of water through the tissue, but, unexpectedly, some deep cells also swell to a proportionately greater volume than surface cells. Conversely, chondrocyte shrinkage occurs in a well-coordinated fashion in all cells when tissue is suspended in hypertonic medium. The results, using the post-regulatory volume decrease/regulatory volume increase protocol (15), show that chondrocytes have some volume regulatory capacity in situ. This is shown by incubating the cartilage initially in hypotonic medium, which causes cell swelling, and then shrinking the cells in hypertonic medium (Fig. 13). The cells quickly regain their initial volume, and this appears to be due, principally, to the activity of the bumetanide-sensitive Na^+-K^+-$2Cl^-$ cotransporter (Errington, unpublished observations), as observed in other cell types (15). In

summary, our integrated CLSM protocol as described here can be used to assess the osmotic responsiveness and volume regulatory capacity of chondrocytes in situ. We aim to use more specific fluorescent probes for 3-D and 4-D confocal imaging of signal transduction processes and membrane transport, together with inhibitors to combine dynamic volume measurements with the dissection of volume regulatory mechanisms. Such a combined physiological imaging approach offers the possibility of giving new insights into these fundamental processes, without the perturbations arising from cell isolation.

We thank Drs. J. Urban and R. Wilkins (Dept. of Physiology, Oxford Univ., UK) for many helpful discussions.

This work was funded by the Wellcome Trust (R. J. Errington and A. C. Hall). N. S. White is a Royal Society Industry Fellow, and J. L. Wood acknowledges Biotechnology and Biological Sciences Research Council for a Graduate Studentship.

Present address of A. C. Hall: Dept. of Physiology, Univ. of Edinburgh, Medical School, Teviot Place, Edinburgh EH8 9AG, UK.

Address for reprint requests: R. J. Errington, Dept. of Cell Physiology, Univ. of Nijmegen, PO Box 9101, 6525 HB Nijmegen, The Netherlands.

Received 3 June 1996; accepted in final form 13 September 1996.

REFERENCES

1. **Adams, D. S.** Mechanisms of cell shape change: the cytomechanics of cellular response to chemical environment and mechanical loading. *J. Cell Biol.* 117: 83–93, 1992.
2. **Beletsky, I. P., and S. R. Umansky.** A new assay for cell death. *J. Immunol. Methods* 134: 201–205, 1990.
3. **Carlsson, K.** The influence of specimen refractive index, detector signal integration, and non-uniform scan speed on the imaging properties in confocal microscopy. *J. Microsc.* 163: 167–178, 1991.
4. **Chacon, E., J. M. Reece, A.-L. Nieminen, G. Zahrebelski, B. Herman, and J. J. Lemasters.** Distribution of electrical potential, pH, free Ca^{2+}, and volume inside cultured adult rabbit cardiac myocytes during chemical hypoxia: a multiparameter digitised confocal microscopic study. *Biophys. J.* 66: 942–952, 1994.
5. **Chen, H., J. R. Swedlow, M. Grote, J. Sedat, and D. A. Agard.** The collection, processing and display of digital three-dimensional images of biological specimens. In: *Handbook of Biological Confocal Microscopy*, edited by J. B. Pawley. New York: Plenum, 1995, p. 197–210.
6. **Deshayes, C. M. P., A. C. Hall, and J. P. G. Urban.** Effect of extracellular osmolarity on porcine articular chondrocyte volume (Abstract). *J. Physiol. (Lond.)* 467: 214P, 1993.
7. **Eggli, P. S., E. B. Hunziker, and R. K. Schenk.** Quantitation of structural features characterising weight- and less-weight-bearing regions in articular cartilage: a stereological analysis of medial femoral condyles in young adult rabbits. *Anat. Rec.* 222: 217–227, 1988.
8. **Farnum, C. E., J. Turgai, and N. J. Wilsman.** Visualisation of living terminal hypertrophic chondrocytes of growth plate cartilage in situ by differential interference contrast microscopy and time-lapse cinematography. *J. Orthop. Res.* 8: 750–763, 1989.
9. **Fricker, M. D., and N. S. White.** Wavelength considerations in confocal microscopy of botanical samples. *J. Microsc.* 166: 29–42, 1992.
10. **Guilak, F.** Volume and surface area measurement of viable chondrocytes in situ using geometric modelling of serial confocal sections. *J. Microsc.* 173: 245–256, 1993.
11. **Hall, A. C.** Volume-sensitive taurine transport in bovine articular chondrocytes *J. Physiol. (Lond.)* 484: 755–766, 1995.
12. **Hell, S., G. Reiner, C. Cremer, and E. H. K. Stelzer.** Abberations in confocal microscopy induced by mismatches in refractive index. *J. Microsc.* 169: 391–405, 1993.
13. **Hodge, W. A., R. S. Fijan, K. L. Carlson, R. G. Burgess, W. H. Harris, and R. W. Mann.** Contact pressures in the human hip joint measured in vivo. *Proc. Natl. Acad. Sci. USA* 83: 2879–2883, 1986.
14. **Hoffmann, E. K., and L. O. Simonsen.** Membrane mechanisms in volume and pH regulation in vertebrate cells. *Physiol. Rev.* 69: 315–382, 1989.
15. **Ince, C., D. L. Ypey, M. M. C. Dieselhoff-den Dulk, J. A. M. Visser, A. De Vos, and R. Van Furth.** Micro-CO_2-incubator for use on a microscope. *J. Immunol. Methods* 60: 269–275, 1983.
16. **Jensen, B. S., F. Jessen, and E. K. Hoffmann.** Na^+, K^+, Cl^- cotransport and its regulation in Ehrlich ascites tumor cells. Ca^{2+}/calmodulin and protein kinase C dependent pathways. *J. Membr. Biol.* 131: 161–178, 1993.
17. **Maroudas, A.** Physio-chemical properties of articular cartilage. In: *Adult Articular Cartilage*, edited by M. A. R. Freeman. London: Pitman Medical, 1979, p. 215–290.
18. **Mow, V. C., M. H. Holmes, and W. M. Lai.** Fluid transport and mechanical properties of articular cartilage: a review. *J. Biomech.* 17: 377–394, 1984.
19. **Muir, H.** The chondrocyte, architect of cartilage. Biomechanics, structure, function and molecular biology of cartilage matrix macromolecules. *Bioessays* 17: 1039–1048, 1995.
20. **Paukkonen, K., K. Selkainaho, J. Jurvelin, and H. J. Helminen.** Morphometry of articular cartilage: a stereological method using light microscopy. *Anat. Rec.* 210: 675–682, 1984.
21. **Roerdink, J. B. T. M., and M. Bakker.** An fft-based method for attenuation correction in fluorescence confocal microscopy. *J. Microsc.* 169: 3–14, 1993.
22. **Slowman, S., and K. D. Brandt.** Composition and glycosaminoglycan metabolism of articular cartilage from habitually loaded and habitually unloaded sites. *Arthritis Rheum.* 29: 88–94, 1986.
23. **Stockwell, R. A.** Cartilage failure in osteoarthritis: relevance of normal structure and function. A review. *Clin. Anat.* 4: 161–191, 1991.
24. **Terasaki, M., and M. E Dailey.** Confocal microscopy of living cells. In: *Handbook of Biological Confocal Microscopy*, edited by J. B. Pawley. New York: Plenum, 1995, p. 327–345.
25. **Tsien, R., and B. J. Bacskai.** Video-rate confocal microscopy. In: *Handbook of Biological Confocal Microscopy*, edited by J. B. Pawley. New York: Plenum, 1995, p. 459–477.
26. **Urban, J. P. G.** The chondrocyte: a cell under pressure. *Br. J. Rheumatol.* 33: 901–908, 1994.
27. **Urban, J. P. G., and A. C. Hall.** Physical modifiers of matrix metabolism. In: *Articular Cartilage and Osteoarthritis*, edited by K. E. Keuttner, R. Schleyerbach, J. G. Peyron, and V. C. Hascall. New York: Raven, 1992, p. 393–406.
28. **Urban, J. P. G., A. C. Hall, and K. Gehl.** Regulation of synthesis in articular chondrocytes by extracellular osmolarity and ionic composition. *J. Cell. Physiol.* 154: 262–270, 1993.
29. **Visser, T. D., J. L. Oud, and G. J. Brakenhoff.** Refractive index and axial distance measurements in 3-D microscopy. *Optik* 90: 17–19, 1992.
30. **Watt, F. M.** The extracellular matrix and cell shape. *Trends Biochem. Sci.* 11: 482–485, 1986.
31. **White, N. S.** Visualisation systems for multidimensional CLSM images. In: *Handbook of Biological Confocal Microscopy*, edited by J. B. Pawley. New York: Plenum, 1995, p. 211–254.
32. **White, N. S., R. J. Errington, M. D. Fricker, and J. L. Wood.** Aberration control in quantitative imaging of botanical specimens by multi-dimensional fluorescence microscopy *J. Microsc.* 181: 99–116, 1996.
33. **White, N. S., and D. M. Shotton.** Confocal scanning microscopy: three-dimensional biological imaging. *Trends Biochem. Sci.* 14: 435–439, 1989.
34. **Wilkins, R. J., and A. C. Hall.** Control of matrix synthesis in isolated bovine chondrocytes by extracellular and intracellular pH. *J. Cell. Physiol.* 164: 474–481, 1995.
35. **Zanetti, M., A. Ratcliffe, and F. M. Watt.** Two sub-populations of differentiated chondrocytes identified with a mono-clonal antibody to keratan sulphate. *J. Cell Biol.* 101: 53–59, 1985.